Band Gaps of the Lead-Free Halide Double Perovskites $Cs_2BiAgCl_6$ and $Cs_2BiAgBr_6$ from Theory and Experiment

Marina R. Filip,[†] Samuel Hillman,[‡] Amir Abbas Haghighirad,[‡] Henry J. Snaith,[‡] and Feliciano Giustino[*,†]

Department of Materials, University of Oxford, Parks Road OX1 3PH, Oxford, UK, and Department of Physics, University of Oxford, Clarendon Laboratory, Parks Road, Oxford OX1 3PU, UK

E-mail: feliciano.giustino@materials.ox.ac.uk

[*]To whom correspondence should be addressed
[†]Department of Materials, Unversity of Oxford
[‡]Department of Physics, University of Oxford

Abstract

The recent discovery of lead-free halide double perovskites with band gaps in the visible represents an important step forward in the design of environmentally-friendly perovskite solar cells. Within this new family of semiconductors, $Cs_2BiAgCl_6$ and $Cs_2BiAgBr_6$ are stable compounds crystallizing in the elpasolite structure. Following the recent computational discovery and experimental synthesis of these compounds, a detailed investigation of their electronic properties is warranted in order to establish their potential as optoelectronic materials. In this work we perform state-of the art many-body perturbation theory calculations and obtain high accuracy band gaps for both compounds. In addition, we synthesize single crystals of $Cs_2BiAgCl_6$ and $Cs_2BiAgBr_6$ which are stable in ambient conditions. We measure their optical band gaps from absorption and photoluminescence and obtain a good agreement with the calculated quasiparticle band gaps.

Table of Contents Image

Keywords: Double halide perovskites, Lead-free perovskites, Electronic structure, Quasiparticle Band Gap

Hybrid organic-inorganic halide perovskites are currently the fastest developing photovoltaic materials.[1–5] Lead-halide perovskites are solution-processable at low-temperatures,[6] exhibit efficient light absorption in the visible,[7] long diffusion lengths, and high mobilities of the photogenerated carriers,[8] as well as the ability to recycle the photons emitted upon radiative recombination.[9] In the last five years, perovskite solar cells based on methylammonium lead-iodide and related materials showed an unparallelled growth in power conversion efficiency,[10–12] up to a certified record exceeding 22%.[13] However, despite this astounding success, perovskite solar cells are also facing important challenges, due to the lack of stability upon prolonged exposure to light, humidity and increased temperatures.[14–20] In addition, the toxicity of lead calls into question the long-term environmental impact of perovskite solar cells.[21–23]

A promising avenue for addressing both the stability and the toxicity bottlenecks is to explore closely-related compounds via rational design. For example, it has been shown that by employing mixed-halide and mixed cation perovskites not only can the electronic properties be tuned,[24–27] but also the composition of the mixes can be explored in order to locate a 'stability sweet-spot'.[28] Similar design principles have been employed in the search for potential Pb-replacements, but materials which can rival the unique optoelectronic properties of lead-halide perovskites have not been found yet. The strategy of completely replacing Pb by Sn has so far been unsuccessful, due to the tendency of Sn to oxidize in the +4 state rather than the desired +2 state.[29,30] Furthermore, recent studies focused on the ecotoxity of Sn perovskites, and suggested that Sn is not likely to mitigate the health hazards of halide perovskite solar cells.[21] In addition, high-throughput computational studies pointed out that the substitution of Pb by other metals in the periodic table is likely to compromise the ideal optoelectronic properties of lead-halide perovskites,[31,32] and demonstrated that lead is key to the electronic properties of these materials.

Very recently, three independent studies reported simultaneously the successful replacement

of Pb via the heterovalent substitution with Bi and Ag,[33–35] so as to form a halide double perovskites. In Ref. 35 we reported the computational design of a new family of halide double perovskites of the type $Cs_2BB'X_6$ (with B = Sb, Bi; B′ = Cu, Ag, Au and X = Cl, Br, I). These compounds exhibit band gaps which are highly tunable in the visible range, as well as low effective masses. The experimental synthesis of two members of this family, $Cs_2BiAgCl_6$ and $Cs_2BiAgBr_6$, was successfully demonstrated,[33–35] both via solid-state reactions and via solution processing. Both compounds crystallize in the elpasolite structure, a highly symmetric face-centered cubic double-perovskite structure, they absorb light in the visible range of the solar spectrum, and exhibit an impressive stability under ambient conditions.[33,35] Shortly after the discovery of $Cs_2BiAgCl_6$ and $Cs_2BiAgBr_6$, the synthesis of hybrid organic-inorganic halide double perovskite $CH_3NH_3BiKCl_6$ was reported,[36] further expanding the potential for materials design in this family of compounds. While photovoltaic devices employing halide double perovskites have not yet been reported, these materials promise to be the long sought-after stable, non-toxic halide perovskites, and warrant a thorough investigation of their optoelectronic properties.

Optical measurements and electronic structure calculations suggest that both $Cs_2BiAgCl_6$ and $Cs_2BiAgBr_6$ are indirect band gap semiconductors.[33–35] However, there are sizeable discrepancies in the measured optical band gaps. The gaps reported for $Cs_2BiAgCl_6$ range from 2.2 eV[35] 2.77 eV,[34] while those of $Cs_2BiAgBr_6$ range from 1.83 eV[33] to 2.19 eV.[34] These differences are possibly due to the different methods of sample preparation (solid state reaction vs. solution processing), and measurement techniques (optical absorption and photoluminescence[33,35] vs diffuse reflectance[34]), but also to the fitting procedures used to determine the indirect band gap from Tauc plots. Since the band gap is a crucial property in the operation of solar cells, these discrepancies call for further investigations. Refs. 34,35 also report on the calculation of the band gaps using density functional theory and the hybrid fuctionals PBE0[37,38] and HSE.[38–40] The calculated band gaps also exhibit significant discrepancies: the values reported for $Cs_2BiAgCl_6$ range from 2.6 eV[34] to 3.0 eV[35] and

those for $Cs_2BiAgBr_6$ range from 2 eV[34] to 2.3 eV.[35] This may be due to the different crystal structures used in the calculations, but also to the known tendency of PBE0 and HSE hybrid functionals to yield band gaps which can differ significantly.[41] Moreover, hybrid functional approaches are strongly dependent on the fraction of exact exchange and hence not fully predictive. In this work we resolve the ambiguity on the determination of the band gap of $Cs_2BiAgCl_6$ and $Cs_2BiAgBr_6$ by performing state-or-the-art many-body perturbation theory calculations in the *GW* approximation.[42–46] In addition, we synthesize $Cs_2BiAgCl_6$ and $Cs_2BiAgBr_6$ and measure their optical band gaps, obtaining a very good agreement with the computed quasiparticle band gaps.

Cs_2BiAgX_6 (X = Cl, Br) crystallizes in the elpasolite K_2NaAlF_6 structure, which corresponds to an ideal double perovskite. This structure is a network of corner-sharing octahedra, with Cs in the middle of the cuboctahedral cavity. The centers of the octahedra are either occupied by Bi or Ag, alternating in a rock-salt configuration, as shown in Figure 1a.

We synthesize crystalline samples of $Cs_2BiAgCl_6$ and $Cs_2BiAgBr_6$ through both an acidic solution process and a solid state reaction route, as described in the Supporting Information. Through these two methods we obtain high-purity pollycrystalline samples, as well as single-phase crystals of up to 1 mm^3 in size (shown in Figure 1c-d), respectively. Our single crystals exhibit very good stability under environmental conditions. We fully characterize their crystal structure through powder and single crystal X-Ray diffraction (XRD) measured at room temperature (Figure S1 of the Supporting Information). For both compounds we find $Fm\bar{3}m$ face-centered cubic structures, and resolve the atomic positions and lattice parameters. Our refinements are in agreement with Refs. 33–35. The primitive unit cells comprise of only one formula unit, as shown in Figure 1b, while the conventional unit cell comprises of four formula units (Figure 1a).

We investigate the electronic structure of both compounds by first calculating the band structures within the local density approximation to density functional theory[47,48] (DFT-LDA,

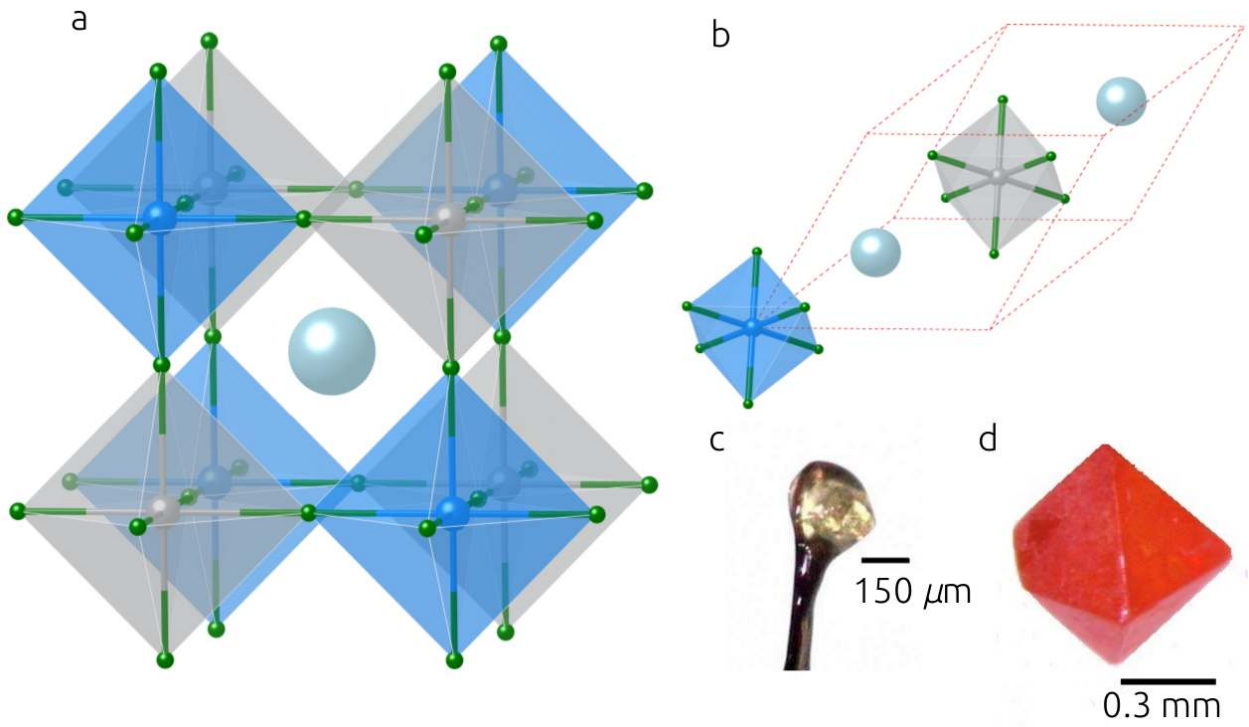

Figure 1: Polyhedral model of (a) the conventional unit cell and (b) the primitive unit cell of Cs_2BiAgX_6 (X = Cl, Br). In (b) the red dashed lines mark the primitive lattice vectors. The large light blue spheres represent the Cs atoms, the small grey, blue and green spheres are the Ag, Bi and halogen atoms, respectively. Single crystal of $Cs_2BiAgCl_6$ (c) and $Cs_2BiAgBr_6$(d), synthesized as described in the Supporting Information.

as described in the Supporting Information), as implemented in the Quantum Espresso suite.[49] In both cases the calculated band gap is indirect, with the valence band top at the X $(2\pi/a, 0, 0)$ point, and the conduction band bottom at the L $(\pi/a, \pi/a, \pi/a)$ point of the Brillouin zone. In Figure 2a and 2b we show a comparison between the band structure of $Cs_2BiAgCl_6$ and $Cs_2BiAgBr_6$ calculated with or without spin-orbit coupling. We observe a large spin-orbit splitting of 2 eV of the first conduction band. The spin-orbit coupling leads to the formation of an isolated conduction band in the middle of the scalar relativistic band gap. Such a large qualitative difference between the scalar-relativistic and the fully-relativistic calculations is reminiscent of lead-halide perovskites, where the spin-orbit coupling is essential for the correct description of the band edges and effective masses.[50,51] In all the following calculations we explicitely take into account spin-orbit coupling.

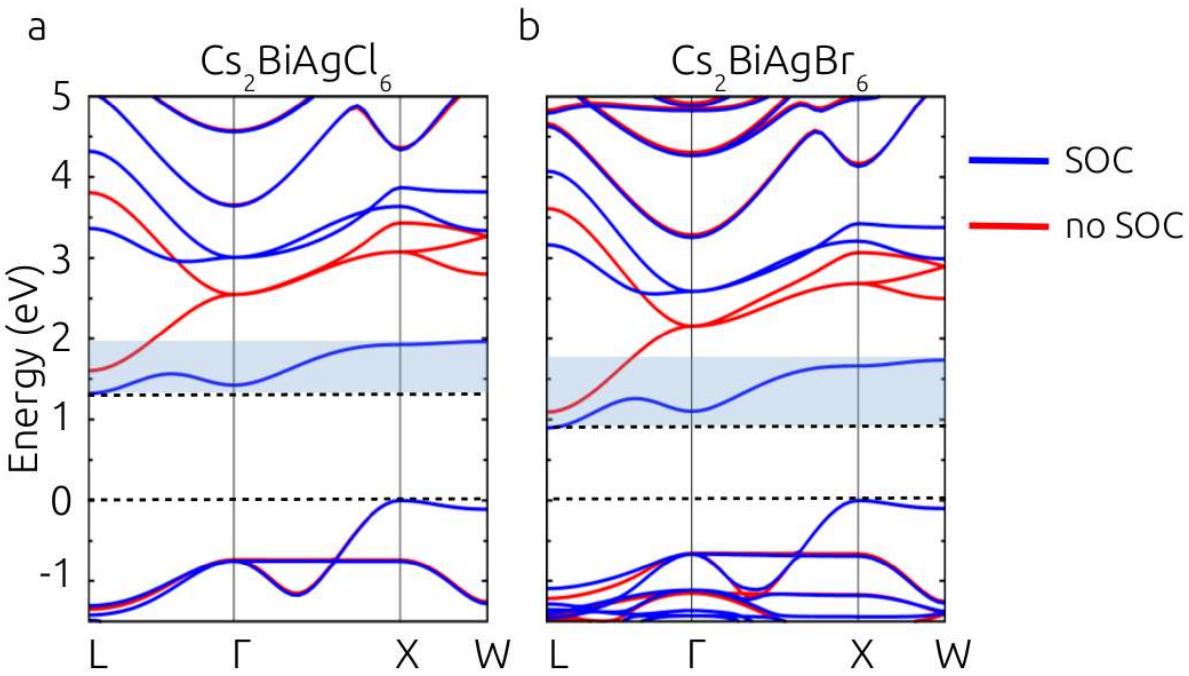

Figure 2: DFT-LDA band structure of $Cs_2BiAgCl_6$ (a) and $Cs_2BiAgBr_6$ (b). The calculations are performed with (blue lines) and without (red lines) spin-orbit coupling. The light blue shading highlights the width of the lowest conduction band as calculated from DFT+SOC: 0.6 eV for $Cs_2BiAgCl_6$ and 0.9 eV for $Cs_2BiAgBr_6$.

As shown in Figure 2, the conduction band bottom in both cases has two minima, with energies within less than 0.2 eV. This small difference is sensitive to the structure of the compound. In Figure S2 of the Supporting Information we show a comparison between the DFT band structures calculated for the experimental and for the optimized structures. In the case of $Cs_2BiAgCl_6$, we can see that the conduction band bottom is either at the Γ or L point, depending on whether calculations are performed on the optimized or the experimental structures. Similar results are obtained in the case of $Cs_2BiAgBr_6$. In order to avoid any ambiguity arising from the sensitivity of the conduction band edge to the crystal structure, in all following calculations we use the experimental crystal structures, with atomic positions and lattice parameters listed in Table S1 and S2 of the Supporting Information.

In order to clarify some of the peculiar features of the band structures of these compounds, we calculate the atom-projected density of states (Figure S3 of the Supporting Information)

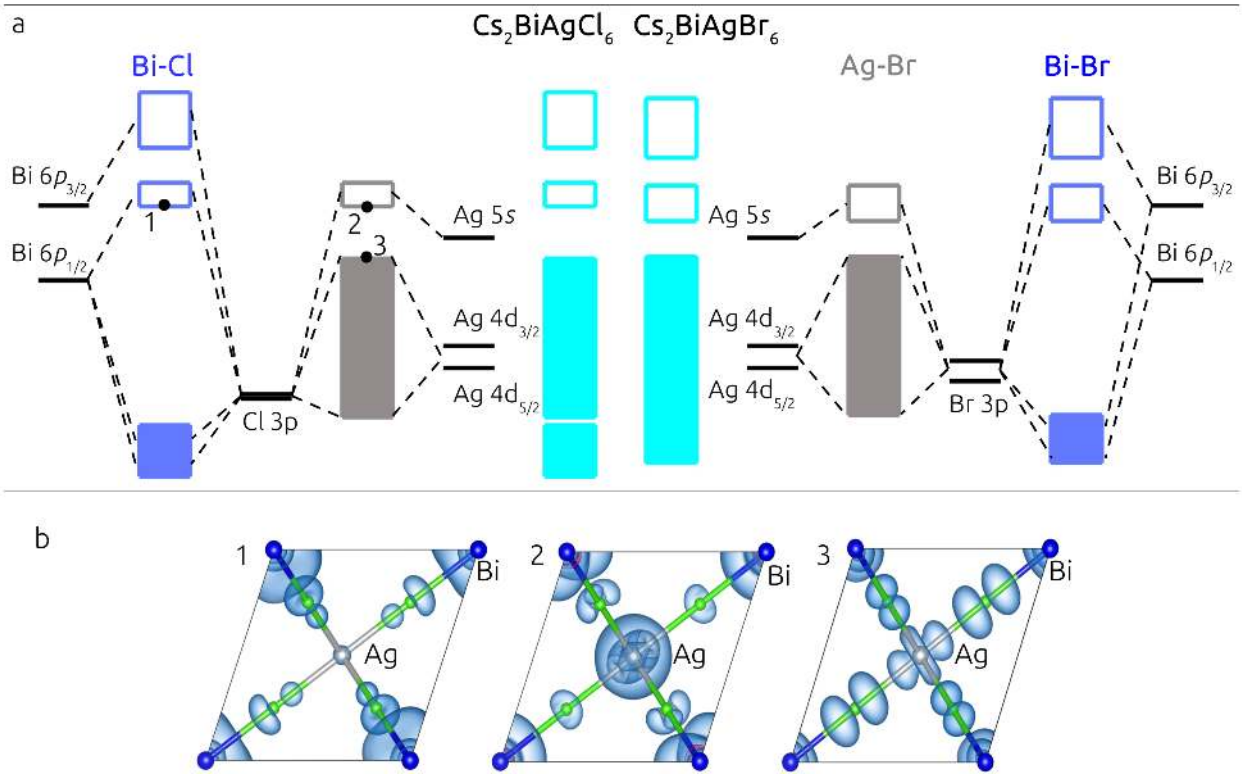

Figure 3: (a) Comparison of the molecular orbital diagrams $Cs_2BiAgCl_6$ (left) and $Cs_2BiAgBr_6$ (right). The atomic one-electron energies are marked by black thick lines, dark blue rectangles correspond to the Bi-halide hybrid bands and the grey rectangles correspond to the Ag-halide hybrid bands. The light blue rectangles represent the bands formed in $Cs_2BiAgCl_6$ and $Cs_2BiAgBr_6$ respectively. Filled rectangles represent occupied (valence) bands, while the empty rectangles represent the unoccupied (conduction) bands. All bands are aligned with respect to the all-electron energy level of the Bi-$5d_{1/2}$ and then red-shifted by 1.5 eV for visualization purposes. (b) Square modulus of the wave functions for states marked from 1 to 3 on the molecular orbital diagram of $Cs_2BiAgCl_6$. 1 represents the Bi-$6p_{1/2}$/halide-p antibonding orbitals at the bottom of the conduction band (at Γ point). 2 is the antibonding Ag-5s/halide-p at the L-point of the conduction band), while 3 corresponds to the Ag-4d/halide-p antibonding orbitals found at the top of the valence band (at X-point). The color codes for the atoms are the same as in Figure 1. In the wave-function plots the Cs atoms are not shown for clarity.

and use this to construct the molecular orbital diagrams of both halide double perovskites. In Figure 3 we show a schematic representation of the bonding and antibonding states in the valence and conduction bands. In both compounds the isolated conduction band originates primarily from spin-orbit coupling, due to a splitting of the Bi-$p_{1/2}$ and Bi-$p_{3/2}$ states in the conduction band (Figure 2 and Figure S3). This band is predominantly antibonding

Bi-p/halogen-p states, and its corresponding bonding orbitals can be found approximately 5 eV below the valence band top in both cases (Figure S3). In addition, a small contribution of the Bi-s/halogen-p antibonding state can be seen at the top of the valence band (diagram 3 in Figure 3b). Hybridized Ag-d/halogen-p states are predominant throughout the highest valence band in both compounds, while the Ag-s states are pushed to the conduction band, consistent with the +1 character of the noble metal in this chemical environment.

From Figure 3 we can rationalize the changes in the electronic structure of the two double perovskites with the halogen atom. As we move from Cl to Br we observe that the valence band width is reduced and the valence band top is slightly higher in energy. The band narrowing is due to the smaller difference in energy between the Ag-d and Br-p levels as compared to Ag-d and Cl-p; the shift to higher energies is due to the fact that the Bi-p states are higher than the Cl-p states. The change in the band gap when moving from Cl to Br is dominated by the increase in the width of the bottom conduction band from 0.6 eV to 0.9 eV (Figure 2). This feature is due to the more delocalized nature of Br-4p orbitals as compared to the Cl-3p states, which increases the overlap with the Bi-6p wave functions, and thereby the dispersion of the conduction bands. In addition, Br-4p levels are shallower and closer in energy to the Bi-6p states than in the case of the Cl-p, leading to a shift of the conduction band to lower energies in the case of $Cs_2BiAgBr_6$.

The electronic structure of the Bi-Ag halide double perovskites exhibits similar features to ternary chalchopyrite semiconductors, $CuInS_2$ (CIS), $CuGaS_2$ (CGS) and also the quaternary Cu_2ZnSnS_4 (CZTS).[52,53] In this family of compounds the noble metal d states are predominant in the valence band and exhibit strong bonds with the chalcogen anions, in close analogy to $Cs_2BiAgCl_6$ and $Cs_2BiAgBr_6$. The anion-p orbitals contribute to both the conduction and valence bands both in the double perovskites (see Figure S2) and in CZTS.[52] In addition, CZTS also exhibits an isolated conduction band, although it corresponds to a Sn-s/S-p character and therefore is not arising from spin-orbit coupling. In fact, the iso-

lated conduction band is a common feature in quaternary compounds, and in particular in elpasolites.[54]

As expected, the band gaps calculated within DFT-LDA including spin-orbit coupling underestimate the optical band gaps reported in Refs 33–35, the discrepancy being as large as 1.6 eV. To correct this severe underestimation, we calculate the GW quasiparticle band gaps of $Cs_2BiAgCl_6$ and $Cs_2BiAgBr_6$ using the `Yambo` code.[55] A detailed report of all convergence tests with respect to the number of empty states, plane-wave cutoffs as well as the Brillouin zone sampling can be found in the Supporting Information (see Figure S4 and S5).

The semicore states $4s^24p^6$ of Ag are particularly important for the calculation of the quasiparticle energies. This is shown in Figure S6 of the Supporting Information, where we compare the quasiparticle energies and the separate contributions from the exchange and correlation self energies calculated using the $4d^{10}5s^1$ and $4s^24p^64d^{10}5s^0$ valence configurations of Ag. Here we see that the quasiparticle band gap increases by 1 eV when the semicore $4s^24p^6$ states of Ag are included in the calculation (Figure S6a). As shown in Figure S6b and S6c, the largest contribution of the semicore states to the quasiparticle correction comes from the exchange term. The correlation self-energy, on the other hand, is virtually unaffected. This effect originates in the large overlap between the $4d^{10}$ orbitals and the $4s^2$ and $4p^6$ orbitals of Ag (see Figure S7 of the Supporting Information, and is more pronounced in the exchange self-energy, which is energy-independent. The contribution of semicore states to the quasiparticle energies is most pronounced at the top of the valence band, where the Ag-$4d$ is predominant (Figure S6). The impact of semicore electrons on the calculation of the exchange self energy is well documented in the literature,[44,56–59] and is known to have a large contribution when d electrons overlap significantly with the s and p electrons of the same shell.[56]

In Figure 4 we plot the direct and indirect band gaps calculated from G_0W_0 along with the measured optical band gaps for $Cs_2BiAgCl_6$ and $Cs_2BiAgBr_6$. For completeness, in Figure 4

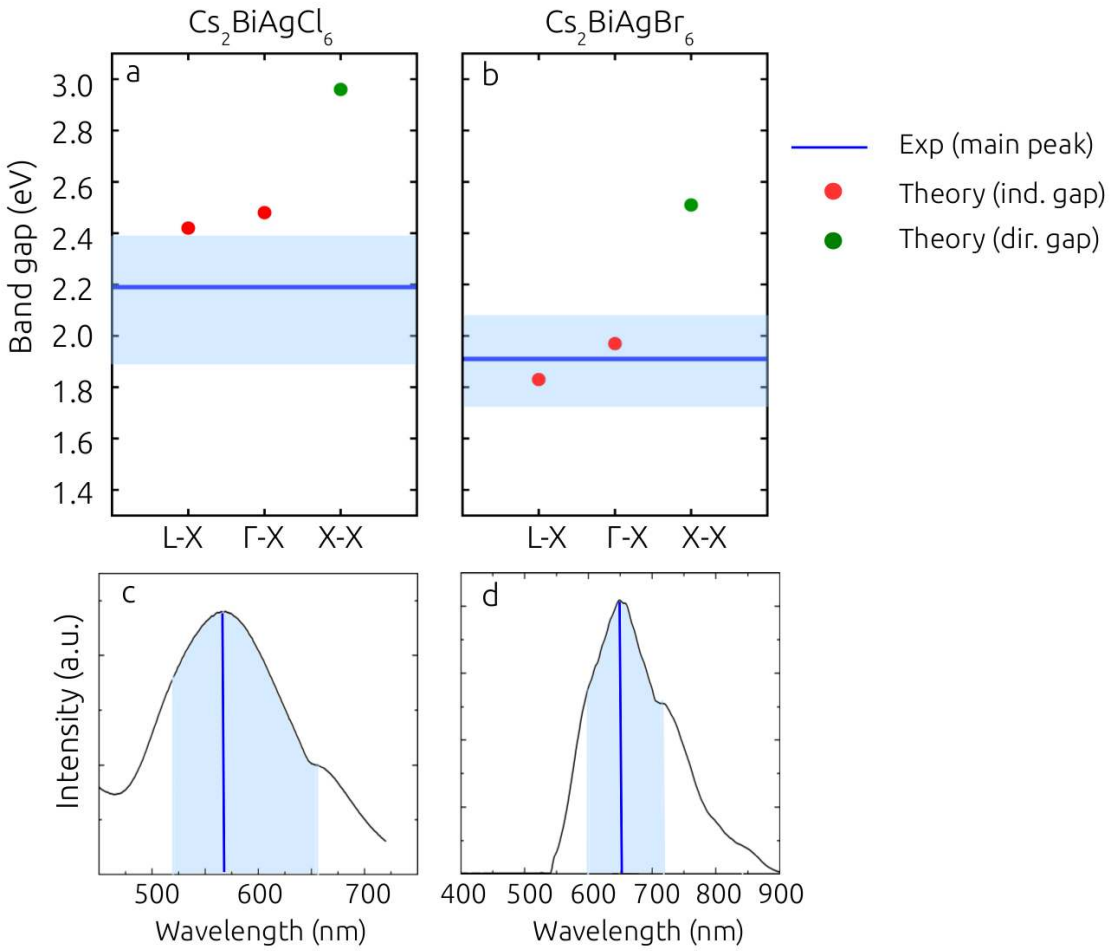

Figure 4: Comparison between the quasiparticle indirect (red disks) and direct band gaps (green disks) and experimental band gaps (blue lines) for $Cs_2BiAgCl_6$ (a) and $Cs_2BiAgBr_6$ (b). The area shaded in light blue is given by the positions of the two shoulders each side of the peaks in the photoluminescence spectra shown in (c) and (d). Room temperature photoluminescence spectra measured for $Cs_2BiAgCl_6$ (c) and $Cs_2BiAgBr_6$ (d). The blue continuous lines mark the positions iof the main peaks in each case, while the light blue shaded area makes the region between the two shoulders located each side of the main peak. The photoluminescence spectrum of $Cs_2BiAgCl_6$ is the same as the one we reported in Figure 2 of Ref. 35.

we report the two lowest computed indirect band gaps between L-X and Γ-X, as well as the computed direct band gap at the X-point. For $Cs_2BiAgCl_6$ we obtain indirect quasiparticle band gaps of 2.42 eV (L-X) and 2.48 eV (Γ-X) and a direct band gap at X of 2.96 eV, while for $Cs_2BiAgBr_6$ we obtain indirect band gaps of 1.83 eV (L-X) and 1.97 eV (Γ-X) and a direct band gap of 2.51 eV. These values are smaller than in the hybrid functional calculations

reported in Ref 34,35 by up to 0.6 eV. The room-temperature photoluminescence (Figure 4) and optical absorption (Figure S8 of the Supporting Information) spectra of $Cs_2BiAgCl_6$ and $Cs_2BiAgBr_6$ are consistent with the indirect character of its band gap, in agreement with Refs 33–35. The main peaks of the photoluminescence spectra are at 567 nm (2.19 eV) for $Cs_2BiAgCl_6$ and 649 nm (1.91 eV) for $Cs_2BiAgBr_6$; this is consistent with the optical absorption spectra shown in Figure S8 of the Supporting Information. Our measured band gap for $Cs_2BiAgBr_6$ is in very good agreement with Ref. 33. By contrast, the indirect band gaps of both $Cs_2BiAgCl_6$ and $Cs_2BiAgBr_6$ reported in Ref. 34 overestimate our results and those of Ref. 33 by up to 0.6 eV. Given these observations, the agreement between the calculated and experimental band gaps reported in Ref. 34 is likely fortuitous.

In both photoluminescence spectra we observe two shoulders on each side of the main peaks, at 520 nm (2.38 eV) and 656 nm (1.89 eV) for $Cs_2BiAgCl_6$ and at 600 nm (2.07) and 718 nm (1.73 eV) for $Cs_2BiAgBr_6$. In both cases the difference between the position of the main peak and the two shoulders is too large to be explained by the absorption or emission of phonons, which have energies in the range of 10 meV.[60] On the other hand, these features are similar to the two indirect optical transitions observed in the temperature-dependent photoluminescence spectra of WSe_2.[61] Therefore, it is possible that the peaks and shoulders in the PL spectra may correspond to multiple indirect transitions, although we cannot exclude that excitonic effects play a role in these features. To account for the the broad PL lineshape in our analysis, in Figure 4c we plot the indirect band gaps obtained from the energies of the main peaks of the photoluminescence spectra (continuous lines), as well as a shading with a width given by the energies of the shoulders on each side of the main peaks, and compare these results with our *GW* band gaps. In general a direct comparison between optical band gaps measured at room temperature and quasiparticle band gaps is not straightforward, due to the absence of excitonic and electron-phonon coupling effects in the *GW* formalism. However, by analogy with the case of $CH_3NH_3PbI_3$, we can expect that these effects will have only a small contribution contribution to the band gap. Indeed,

in the case of $CH_3NH_3PbI_3$, the excitonic effects are bellow 50 meV,[62,63] while increasing temperature opens the band gap by up to at 50-60 meV within the same crystal phase.[64] These two small effects tend to cancel each other, therefore it is meaningful to compare the experimental optical band gaps and calculated quasiparticle band gaps.[59]

Figure 4 shows that our calculated quasiparticle band gaps are in good agreement with the optical measurements for the two double perovskites. The indirect quasiparticle band gaps of $Cs_2BiAgCl_6$ overestimates the optical band gap range obtaind from photoluminescence by approximately 0.2 eV, while in the case of $Cs_2BiAgBr_6$, the two indirect band gaps are within less than 0.1 eV from the optical band gap. These small discrepancies could be due to local changes in the crystal structure which can affect the measured band gaps; in particular, local structural distortions should have a stronger effect for $Cs_2BiAgCl_6$ than for $Cs_2BiAgBr_6$. This hypothesis is supported by the analysis of the band structures calculated for experimental and optimized crystal structures shown in Figure S2; the band gap variation calculated in the case of $Cs_2BiAgCl_6$ (0.33 eV) is twice as large as the one calculated for $Cs_2BiAgBr_6$ (0.16 eV).

In conclusion, we have presented a detailed study of the electronic properties of the newly discovered $Cs_2BiAgCl_6$ and $Cs_2BiAgBr_6$ halide double perovskites within DFT+SOC and state-of-the-art *GW* quasiparticle calculations. We have synthesized $Cs_2BiAgCl_6$ and $Cs_2BiAgBr_6$ single crystals and performed optical absorption and photoluminescence measurements. Our analysis of the electronic structure revealed that the two halide double perovskites are indirect band gap semiconductors with electronic properties which resemble closely the well known lead-halide perovskites as well as the ternary and quaternary chalchopiryte semiconductors of the CIGS and CZTS family. We have calculated the quasiparticle band gaps of both compounds with high accuracy and obtained indirect gaps of 2.4 eV for $Cs_2BiAgCl_6$ and 1.8 eV $Cs_2BiAgBr_6$. These values are in very good agreement with our experimental band gaps of 2.2 eV and 1.9 eV for $Cs_2BiAgCl_6$ and $Cs_2BiAgBr_6$ respectively.

Future studies should address the optical, excitonic and transport properties properties, as well as the temperature dependence of the structural and electronic properties of these new compounds, in order to fully assess their potential as photovoltaic materials. By following the same materials design strategies currently used for lead-halide perovskites, we believe that it will be possible to optimize the optoelectronic properties this new class of stable and environmentally-friendly perovskites for optoelectronic applications.

Acknowledgement

The research leading to these results has received funding from the the Graphene Flagship (EU FP7 grant no. 604391), the Leverhulme Trust (Grant RL-2012-001), the UK Engineering and Physical Sciences Research Council (Grant No. EP/J009857/1), and the European Union Seventh Framework Programme (FP7/2007-2013) under grant agreements n°239578 (ALIGN) and n°604032 (MESO). The authors acknowledge the use of the University of Oxford Advanced Research Computing (ARC) facility (http://dx.doi.org/10.5281/zenodo.22558) and the ARCHER UK National Supercomputing Service under the 'AMSEC' Leadership project. Figures involving atomic structures were rendered using VESTA.[65]

References

(1) Green, M.; Ho-Baillie, A.; Snaith, H. J. The Emergence of Perovskite Solar Cells. *Nature Photonics* **2014**, *8*, 506.

(2) Green, M. A.; Emery, K.; Hishikawa, Y.; Warta, W.; Dunlop, E. D. Solar Cell Efficiency Tables (Version 45). *Progress in Photovoltaics* **2015**, *23*, 1.

(3) Stranks, S.; Snaith, H. J. Metal-Halide Perovskites for Photovoltaic and Light-Emitting Devices. *Nature Nanotechology* **2015**, *10*, 391.

(4) Seo, J.; Noh, J. H.; Seok, S. I. Rational Strategies for Efficient Perovskite Solar Cells. *Acc. Chem. Res.* **2016**, *49*, 562–572.

(5) Choi, J. J.; Billinge, S. J. L. Perovskites at the Nanoscale: From Fundamentals to Applications. *Nanoscale* **2016**, *8*, 6206–6208.

(6) You, J.; Hong, Z.; Yang, Y. M.; Chen, Q.; Cai, M.; Song, T. B.; Chen, C. C.; Lu, S.; Liu, Y.; Zhou, H.; Yang, Y. Low-Temperature Solution Processed Perovskite Solar Cells with High Efficiency and Flexibility. *ACS Nano* **2014**, *8*, 1674–1680.

(7) De Wolf, S.; Holovsky, J.; Moon, S.-J.; Löpert, P.; Niesen, B.; Ledinsky, M.; Haug, F.-J.; Yum, J.-H.; Ballif, C. Organometallic Halide Perovskites: Sharp Optical Absorption Edge and Its Relation to Photovoltaic Performance. *J. Phys. Chem. Lett.* **2014**, *5*, 1035–1039.

(8) Herz, L. M. Charge-Carrier Dynamics in Organic-Inorganic Metal Halide Perovskites. *Annu. Rev. Phys. Chem.* **2016**,

(9) Pazos-Outón, L. M.; Szumilo, M.; Limboll, R.; Richter, J. M.; Crespo-Quesada, M.; Adbi-Jalebi, M.; Beeson, H. J.; Vrućnić, M.; Alsari, M.; Snaith, H. J.; Ehrler, B.; Friend, R. H.; Deschler, F. Photon Recycling in Lead-Iodide Perovskite Solar Cells. *Science* **2016**, *351*, 1430–1433.

(10) Lee, M. M.; Teuscher, J.; Miyasaka, T.; Myrakami, T. N.; Snaith, H. J. Efficient Hybrid Solar Cells Based on Meso-Superstructured Organometal Halide Perovskites. *Science* **2012**, *338*, 643.

(11) Kim, H.-S.; Lee, C. R.; Im, J.-H.; Lee, K.-B.; Moehl, T.; Marchioro, A.; Moon, S.-J.; Humphry-Baker, R.; Yum, J.-H.; Moser, J. E.; M., G.; N.-G., P. Lead Iodide Perovskite Sensitized All-Solid-State Submicron Thin Film Mesoscopic Solar Cell with Efficiency Exceeding 9%. *Sci. Rep.* **2012**, *2*, 591.

(12) Burschka, J.; Pellet, N.; Moon, S.-J.; Humphry-Baker, R.; Gao, P.; Nazeeruddin, M. K.; Grätzel, M. Sequential Deposition as a Route to High-Performance Perovskite-Sensitized Solar Cells. *Nature* **2013**, *499*, 316.

(13) Best Research-Cell Efficiencies. `http://www.nrel.gov/ncpv/images/efficiency_chart.jpg`.

(14) Niu, G.; Guo, X.; Wang, L. Review of Recent Progress in Chemical Stability of Perovskite Solar Cells. *J. Mater. Chem. A* **2015**, *3*, 8970–8980.

(15) Divitini, G.; Cacovich, S.; Matteocci, F.; Di Carlo, A.; Ducati, C. In Situ Observation of Heat-Induced Degradation of Perovskite Solar Cells. *Nature Energy* **2016**, *1*, 15012.

(16) Li, X.; Dar, M. I.; Yi, C.; Luo, J.; Tschumi, M.; Zakeeruddin, S. M.; Nazeeruddin, M. K.; Han, H.; Grätzel, M. Improved Performance and Stability of Perovskite Solar Cells by Crystal Crosslinking with Alkylphosphonic Acid ω-Ammonium Chlorides. *Nature Chemistry* **2015**, *7*, 703–711.

(17) Sutton, R. J.; Eperon, G. E.; Miranda, L.; Parrott, E. S.; Kamino, B. A.; Patel, J. B.; Hörantner, M. T.; Johnston, M. B.; Haghighirad, A. A.; Moore, D. T.; Snaith, H. J. Bandgap-Tunable Cesium Lead Halide Perovskites with High Thermal Stability for Efficient Solar Cells. *Adv. Energ. Mater.* **2016**,

(18) Manser, J. S.; Saidaminov, M. I.; Christians, J. A.; Bakr, O. M.; Kamat, P. V. Making and Breaking of Lead-Halide Perovskites. *Acc. Chem. Res.* **2016**,

(19) Hoke, E. T.; Slotcavage, D. J.; Dohner, E. R.; Bowring, A. R.; Karunadasa, H. I.; McGehee, M. D. Reversible Photo-Induced Trap Formation in Mixed-Halide Hybrid Perovskites for Photovoltaics. *Chem. Sci.* **2015**, *6*, 613–617.

(20) Eames, C.; Frost, J. M.; Barnes, P. R. F.; O'Regan, A., B. C.and Walsh; Saiful Islam, M.

Ionic Transport in Hybrid Lead Iodide Perovskite Solar Cells. *Nature Commun.* **2015**, *6*, 7497.

(21) Babagayigit, A.; Thanh, D. D.; Ethirajan, A.; Manca, J.; Muller, M.; Boyen, H.-G.; Conings, B. Assessing the Toxicity of Pb- and Sn-Based Perovskite Solar Cells in Model Organism Danio Rerio. *Sci. Rep.* **2016**, *6*, 18721.

(22) Babagayigit, A.; Ethirajan, A.; Muller, M.; Conings, B. Toxicity of Organometal Halide Perovskite Solar Cells. *Nature Materials* **2016**, *15*, 247.

(23) Benmessaoud, I. R.; Mahul-Mellier, A.-L.; Horváth, E.; Maco, B.; Spina, M.; Lashuel, L., H. A. Forró Health Hazards of Methylammonium Lead Iodide Based Perovskites: Cytotoxicity Studies. *Toxicol. Res.* **2016**, *5*, 407–419.

(24) Filip, M. R.; Eperon, G.; Snaith, H. J.; Giustino, F. Steric Engineering of Metal-Halide Perovskites with Tunable Optical Band Gaps. *Nature Commun.* **2014**, *5*, 5757.

(25) Pellet, N.; Gao, P.; Gregori, G.; Yang, T.-Y.; Nazeerrudin, M. K.; Maier, J.; Grätzel, M. Mixed-Organic-Cationic Perovskite Photovoltaics for Enhanced Solar-Light Harvesting. *Angew. Chem.* **2014**, *53*, 3151.

(26) Eperon, G. E.; Stranks, S. D.; Menelaou, C.; Johnston, M.; Hertz, L. M.; Snaith, H. J. Formamidinium Lead Trihalide: A Broadly Tunable Perovskite Heterojunction Solar Cells. *Energ. Environ. Sci.* **2014**, *7*, 982.

(27) Noh, J. H.; Im, S. H.; Heo, T. N., J. H. end Mandal; Seok, S. I. Chemical Management for Colorful, Efficient and Stable Inorganic-Organic Hybrid Nanostructured Solar Cells. *Nano Lett.* **2013**, *13*, 1764.

(28) McMeekin, D. P.; Sadoughi, G.; Rehman, W.; Eperon, G.; Saliba, M.; Hörantner, M. T.; Haghighirad, A.; Sakai, N.; Korte, L.; Rech, B.; Johnston, M. B.; Herz, L. M.;

Snaith, H. J. A Mixed-Cation Lead Mixed-Halide Perovskite Absorber for Tandem Solar Cells. *Science* **2016**, *351*, 151–155.

(29) Hao, F.; Stoumpos, C. C.; Cao, D. H.; Chang, R. P. H.; Kanatzidis, M. G. Lead-free Solid-State Organic-Inorganic Halide Perovskite Solar Cells. *Nature Photonics* **2014**, *8*, 489.

(30) Noel, N.; Stranks, S. D.; Abate, A.; Wehrenfennig, C.; Guarnera, S.; Haghighirad, A.-A.; Sadhanala, A.; Eperon, G. E.; Pathak, S. K.; Johnston, A., M. B. andPetrozza; Herz, L. M.; Snaith, H. J. Lead-Free Organic-Inorganic Tin Halide Perovskite for Photovoltaic Applications. *Energ. Environ. Sci* **2014**, *7*, 3061.

(31) Filip, M. R.; Giustino, F. Computational Screening of Homovalent Lead Substitution in OrganicInorganic Halide Perovskites. *J. Phys. Chem. C* **2016**, *120*, 166–173.

(32) Körbel, S.; Marques, M. A. L.; Botti, S. Stability and Electronic Properties of New Inorganic Perovskites from High-Throughput Ab Initio Calculations. *J. Mater. Chem. C* **2016**,

(33) Slavney, A. H.; Hu, T.; Lindenberg, A. M.; Karunadasa, H. I. A Bismuth-Halde Double Perovskite with Long Carrier Recombination Lifetime for Photovoltaic Applications. *J. Am. Chem. Soc.* **2016**, *138*, 2138–2141.

(34) McClure, E. T.; Ball, M. R.; Windl, W.; Woodward, P. M. Cs_2AgBiX_6 (X = Br, Cl): New Visible Light Absorbing, Lead-Free Halide Perovskite Semiconductors. *Chem. Mater.* **2016**, *28*, 1348–1354.

(35) Volonakis, G.; Filip, M. R.; Haghighirad, A. A.; Sakai, N.; Wenger, B.; Snaith, H. J.; Giustino, F. Lead-Free Halide Double Perovskites via Heterovalent Substitution of Noble Metals. *J. Phys. Chem. Lett.* **2016**, *7*, 1254–1259.

(36) Wei, F.; Deng, Z.; Sun, S.; Xie, F.; Evans, D. M.; Carpenter, M. A.; Bristowe, P. D.; Cheetham, A. K. The Synthesis, Structure and Electronic Properties of a Lead-Free Hybrid Inorganic-Organic Double Perovskite $(MA)_2KBiCl_6$ (MA = methylammonium). *Materials Horizons* **2016**,

(37) Perdew, J. P.; Burke, K.; Ernzerhof, M. Generalized gradient approximation made simple. *Phys. Rev. Lett.* **1996**, *77*, 3865.

(38) Paier, J.; Hirschl, R.; Marsman, M.; Kresse, G. The Perdew-Burke-Ernzerhof exchange-correlation functional applied to the G2-1 test set using a plane-wave basis set. *J. Chem. Phys.* **2005**, *122*, 234102.

(39) Heyd, J.; Scuseria, G. E.; Ernzerhof, M. Hybrid Functionals Based on a Screened Coulomb Potential. *J. Chem. Phys.* **2003**, *118*, 8207–8215.

(40) Heyd, J.; Scuseria, G. E.; Erzerhof, M. Hybrid Functionals Based on a Screened Coulomb Potential. *J. Chem. Phys.* **2006**, *124*, 219906.

(41) Friedrich, C.; Betzinger, M.; Schlipf, M.; Blügel, S.; Schindlmayr, A. Hybrid functionals and *GW* approximation in the FLAPW method. *J. Phys. Condens. Matter* **2012**, *24*, 293201.

(42) Hedin, L. New Method for Calculating the One-Particle Green's Function with Application to the Electron-Gas Problem. *Phys. Rev.* **1965**, *139*, A796.

(43) Hybertsen, M. S.; Louie, S. G. Electron Correlation in Semiconductors and Insulators: Band Gaps and Quasiparticle Energies. *Phys. Rev. B* **1986**, *34*, 5390.

(44) Aryasetiawan, F.; Gunnarsson, O. The *GW* Method. *Rep. Prog. Phys.* **1998**, *61*, 237.

(45) Giustino, F.; Cohen, M. L.; Louie, S. G. *GW* Method with the Self-Consistent Sternheimer Equation. *Phys. Rev. B* **2010**, *81*, 115105.

(46) Onida, G.; Reining, L.; Rubio, A. Electronic Excitations: Density-Functional Versus Many-Body Green's Function Approaches. *Rev. Mod. Phys.* **2002**, *74*, 601–659.

(47) Hohenberg, P.; Kohn, W. Inhomogeneous Electron Gas. *Phys. Rev.* **1964**, *136*, B864.

(48) Perdew, J. P.; Zunger, A. Self-Interaction Correction to Density-Functional Approximations for Many-Electrons Systems. *Phys. Rev. B* **1981**, *23*, 5048.

(49) Gianozzi, P.; Baroni, S.; Bonini, N.; Calandra, M.; Car, R.; Cavazzoni, C.; Ceresoli, D.; Chiarotti, G. L.; Cococcioni, M.; Dabo, I.; Dal Corso, A.; de Gironcoli, S.; Fabris, S.; Fratesi, G.; Gebauer, R. et al. QUANTUM ESPRESSO: A Modular and Open-Source Software Project for Quantum Simulations of Materials. *J. Phys.: Condens. Matter.* **2009**, *21*.

(50) Filip, M. R.; Verdi, C.; Giustino, F. GW Band Structures and Carrier Effective Masses of CH3NH3PbI3 and Hypothetical Perovskites of the Type APbI3: A = NH4, PH4, AsH4 and SbH4. *J. Phys. Chem. C* **2015**, *119*, 25209–25219.

(51) Menéndez-Proupin, E.; Palacios, P.; Wahnón, P.; Conesa, J. C. Self-Consistent Relativistic Band Structure of the $CH_3NH_3PbI_3$ Perovskite. *Phys. Rev. B* **2014**, *90*, 045207.

(52) Paier, J.; Asahi, R.; Nagoya, A.; Kresse, G. Cu_2ZnSnS_4 as a potential photovoltaic material: A hybrid Hartree-Fock density functional study. *Phys. Rev. B* **2009**, *79*, 115126.

(53) Jaffe, J. E.; Zunger, A. Theory of the band gap anomaly in ABC_2 chalcopyrite semiconductors. *Phys. Rev. B* **1984**, *29*, 1882.

(54) Shi, H.; Du, M.-H. Discrete Electronic Bands in Semiconductors and Insulators: Potential High-Light-Yield Scintillators. *Phys. Rev. Appl.* **2015**, *3*, 054005.

(55) Marini, A.; Hogan, C.; Grüning, M.; Varsano, D. Yambo: An Ab Initio Tool for Excited State Calculations. *Comp. Phys. Commun.* **2009**, *180*, 1392.

(56) Rohlfing, M.; Krüger, P.; Pollmann, J. Quasiparticle band structure of CdS. *Phys. Rev. Lett.* **1995**, *75*, 3489.

(57) Marini, A.; Onida, G.; Del Sole, R. Quasiparticle Electronic Structure of Copper in the *GW* approximation. *Phys. Rev. Lett.* **2002**, *88*, 016403–1.

(58) Filip, M. R.; Patrick, C. E.; Giustino, F. GW Quasiparticle Band Structures of Stibnite, Antimonselite, Bismuthinite, and Guanajuatite. *Phys. Rev. B* **2013**, *87*, 205125.

(59) Filip, M. R.; Giustino, F. GW Quasiparticle Band Gap of the Hybrid Organic-Inorganic Perovskite CH3NH3PbI3: Effect of Spin-Orbit Interaction, Semicore Electrons, and Self-Consistency. *Phys. Rev. B* **2014**, *90*, 245145.

(60) Perez-Osoório, M. A.; Millot, R. L.; Filip, M. R.; Patel, J. B.; Herz, L. M.; Johnston, M. B.; Giustino, F. Vibrational Properties of Organic-Inorganic Halide Perovskite $CH_3NH_3PbI_3$ from Theory and Experiment: Factor Group Analysis, First Principles Calculations and Low-Temperature Infrared Spectra. *J. Phys. Chem. C* **2015**, *119*, 25703–25718.

(61) Zhao, W.; Ribeiro, R. M.; Toh, M.; Carvalho, A.; Kloc, C.; Castron Neto, A. H.; Eda, G. Origin of the Indirect Optical Transitions in Few-Layer MoS_2, WS_2 and WSe_2. *Nano Letters* **2013**, *13*, 5267–5634.

(62) D'Innocenzo, V.; Grancini, G.; Alcocer, M. J. P.; Kandada, A. R. S.; Stranks, S. D.; Lee, M. M.; Lanzani, G. L.; Snaith, H. J.; Petrozza, A. Excitons versus Free Charges in Organo-Lead Tri-Halide Perovskites. *Nature Commun.* **2014**, 3586.

(63) Myiata, A.; Mitiogly, A.; Plochocka, P.; Portugall, O.; Wang, J. T.-W.; Stranks, S. D.; Snaith, H. J.; Nicholas, R. J. Direct Measurement of the Exciton Binding Energy and Effective Masses for Charge Carriers in Organic-Inorganic Tri-Halide Perovskites. *Nature Physics* **2015**, *11*, 582–587.

(64) Millot, R. L.; Eperon, G. E.; Snaith, H. J.; Johnston, M. B.; Herz, L. M. Temperature-Dependent Charge-Carrier Dynamics in $CH_3NH_3PbI_3$ Perovskite Thin Films. *Adv. Func. Mater.* **2015**, *25*, 6218–6227.

(65) Momma, K.; Izumi, F. VESTA: A Three-Dimensional Visualization System for Electronic and Structural Analysis. *J. Appl. Cryst.* **2008**, *41*, 653.

Band Gaps of the Lead-Free Halide Double Perovskites $Cs_2BiAgCl_6$ and $Cs_2BiAgBr_6$ from Theory and Experiment

Supporting Information

Marina R. Filip,[†] Samuel Hillman,[‡] Amir Abbas Haghighirad,[‡] Henry J. Snaith,[‡] and Feliciano Giustino[*,†]

Department of Materials, University of Oxford, Parks Road OX1 3PH, Oxford, UK, and Department of Physics, University of Oxford, Clarendon Laboratory, Parks Road, Oxford OX1 3PU, UK

E-mail: feliciano.giustino@materials.ox.ac.uk

[*]To whom correspondence should be addressed
[†]Department of Materials, Unversity of Oxford
[‡]Department of Physics, University of Oxford

Computational Setup

Band structure and density of states calculations. All density functional theory calculations are performed within the local density approximation (LDA),[1] as implemented in the `Quantum Espresso` suite.[2] Band structures are calculated with and without spin-orbit coupling effects, using ultrasoft pseudopotentials[3] including non-linear core correction[4] for Bi, Ag, Cl and Br, as found in the Theos Library.[5] For Cs we use the norm-conserving non-relativistic pseudopotential in the Quantum Espresso Library. For the projected density of states we sample the Brillouin zone using a dense $20 \times 20 \times 20$ k-point grid in both cases. The molecular orbital diagrams shown in Figure 2a are built using the data obtained from the projected density of states calculations. For the band structure and projected density of states calculations we use plane-wave cutoffs of 60 Ry and 300 Ry for the wave functions and charge density respectively.

Ground state calculations. For the calculation of the single particle energies, we use norm-conserving[6] pseudopotentials. For Cs and Cl we use non-relativistic pseudopotentials (as found in the Quantum Espresso library) as we do not expect the spin-orbit coupling effects to be significant for these ions. In the case of Bi, Ag and Br we generated a set of fully relativistic, Troullier-Martins norm conserving pseudopotentials[6] using the `ld1.x` code of the Quantum Espresso distribution. For these ions we consider the following electronic configurations: $5d^{10}6s^26p^3$ (Bi), $4s^24p^64d^{10}5s^0$ (Ag) and $3d^{10}4s^24p^5$ (Br). In order to show the importance of semicore electrons for GW calculations we also generate a pseudopotential of Ag with the $4d^{10}5s^1$ cofiguration. Unless othewise specified, all calculations are performed including semicore states for Ag. The charge density is calculated using a large plane wave cutoff of 300 Ry and a $10\times10\times10$ Γ-centered k-point grid in order to sample the Brillouin zone.

Quasiparticle energies. The quasiparticle energies can be calculated from many-body perturbation theory as: $E_{n\mathbf{k}} = \epsilon_{n\mathbf{k}} + Z(\epsilon_{n\mathbf{k}})\langle n\mathbf{k}|\Sigma_{n\mathbf{k}}(\epsilon_{n\mathbf{k}}) - V_{\rm xc}|n\mathbf{k}\rangle$,[7–10] where $\epsilon_{n\mathbf{k}}$ are the Kohn-

Sham eigenvalues for band n and wave-vector $\mathbf{k}$, $E_{n\mathbf{k}}$ are the corresponding eigenvalues, $\Sigma(\omega)$ is the frequency-dependent self-energy, $Z(\omega) = [1 - \mathrm{Re}(\partial\Sigma/\partial\omega)]^{-1}$ is the quasiparticle renormalization, and V_{xc} is the exchange and correlation potential. The self-energy is calculated within the G_0W_0 approximation as $\Sigma = \mathrm{i}G_0W_0$, where G_0 is the single-particle Green's function and W_0 is the screened Coulomb interaction. The self energy is typically separated into two terms, the energy-independent exchange self energy, Σ_{x}, and the energy dependent correlation self energy, Σ_{c}.[7–10]

For the calculation of the quasiparticle eigenvalues we use the G_0W_0 approximation as implemented in the `Yambo` code.[11] We calculate the dielectric matrix within the random phase approximation[12,13] and model its frequency dependence within the Godby-Needs plasmon pole approximation.[14] We use a plane wave cutoff of 50 Ry to calculate the exchange part of the self-energy.

In Figures S4 and S5 we show the convergence with respect to the empty states and polarizability cutoff of the direct band gaps calculated at the Γ-point for $Cs_2BiAgCl_6$ and $Cs_2BiAgBr_6$ respectively. We have also checked that the indirect band gaps follow a similar convergence trend. We define the empty states cutoff as the energy of the highest band included in the summation over empty states with respect to the valence band top at the Γ-point. The rightmost points in Figures S4a and and S5a correspond to calculations which include 1000 total bands (906 empty states in the case of $Cs_2BiAgCl_6$ and 856 empty states in the case of $Cs_2BiAgBr_6$). We find that the band gap converges within 20 meV for 600 bands and 95 eV cutoff in both cases. In addition, we test the convergence with respect to the **k**-point mesh. We obtain that the band gap of $Cs_2BiAgCl_6$ changes by 10 meV when we increase the density of the **k**-point mesh from a $4 \times 4 \times 4$ grid to a $5 \times 5 \times 5$ grid.

The final set of parameters used for our best converged calculation is: 50 Ry plane-wave cutoff for the exchange self energy, 600 bands, 95 eV plane-wave cutoff for the polarizability and a $4 \times 4 \times 4$ **k**-point mesh centered at Γ.

Experimental Methods

Solution-based synthesis and crystal growth of Cs_2BiAgX_6 (X = Cl, Br). Samples of Cs_2BiAgX_6 (X= Cl, Br) were prepared by precipitation from an acidic solution of hydrochloric and hydrobromic acid. A mixture of a 1 mmol $BiBr_3$ (Sigma Aldrich, 99.99%) and AgBr (Sigma Aldrich, 99%) were first dissolved in 12 ml 8.84 M HBr. 2 mmol of CsBr (Sigma Aldrich, 99.9%) were added and the solution was heated to 150°C to dissolve the salts. The solution was cooled to 118°C at 4°C/hour to initiate supersaturation and produce single crystals. The chlorine compound $Cs_2BiAgCl_6$ was fabricated using similar solution method with hydrochloric acid, $BiCl_3$ and CsCl.

High-purity polycrystalline samples were synthesised following the method used by Morss et al.[15] A mixture of 8 ml (8.84 M) HBr and 2 ml 50 wt% H_3PO_2 solution was heated to 120°C and 1.31 mmol of AgBr and $BiBr_3$ dissolved into it. Adding 2.82 mmol of CsBr caused an orange precipitate to form immediately. The hot solution was left for 30 minutes under gentle stirring to ensure a complete reaction before being filtered and the resulting solid washed with ethanol and dried in a furnace.

Synthesis via solid-state reaction. Single-phase samples of Cs_2BiAgX_6 (X = Cl, Br) were prepared by conventional solid-state reaction in a sealed fused silica ampoule.[16] For a typical reaction, the starting materials CsCl, CsBr (Sigma Aldrich, 99.9%), $BiCl_3$, $BiBr_3$ (Sigma Aldrich, 99.99%) and AgCl, AgBr (Sigma Aldrich, 99%) were mixed in a molar ratio 2:1:1, respectively. The mixture was loaded in a fused silica ampoule that was flame sealed under vacuum (10-3 Torr). The mixture was heated to 500°C over 5 hours and held at 500°C for 4 hours. After cooling to room temperature, a yellow and orange polycrystalline material was formed for $Cs_2BiAgCl_6$ and $Cs_2BiAgBr_6$, respectively. Octahedral shaped crystals of maximum size 1 mm^3 could be extracted from the powder samples that later were used to determine the crystal structures.

Structural characterization. Powder X-ray diffraction was carried out using a Panalytical

X′pert powder diffractometer (Cu-$K_{\alpha 1}$ radiation; λ = 154.05 pm) at room temperature. Structural parameters were obtained by Rietveld refinement using General Structural Analysis Software.[17] Single crystal data were collected for $Cs_2BiAgCl_6$ and $Cs_2BiAgBr_6$ at room temperature using an Agilent Supernova diffractometer that uses Mo K_α beam with λ = 71.073 pm and is fitted with an Atlas detector. Data integration and cell refinement was performed using CrysAlis Pro Software (Agilent Technologies Ltd., Yarnton, Oxfordshire, England). The structure was analysed by Patterson and Direct methods and refined using SHELXL 2014 software package.[18]

Optical characterization. A Varian Cary 300 UV-Vis spectrophotometer with an integrating sphere was used to acquire absorbance spectra and to account for reflection and scattering. A 397.7 nm laser diode (Pico-Quant LDH P-C-405) was used for photoexcitation and pulsed at frequencies ranging from 1-80 MHz. The steady-state photoluminescence (PL) measurements were taken using an automated spectrofluorometer (Fluorolog, Horiba Jobin-Yvon), with a 450 W-Xenon lamp excitation.

Table S1: Crystallographic data for a $Cs_2BiAgCl_6$ single crystal. The refinement data are the same as those we reported in Table S1 of the Supporting Information of Ref.[16]

Compound	$Cs_2BiAgCl_6$
Measurement temperature	293 K
Crystal system	Cubic
Space group	$Fm\bar{3}m$
Unit cell dimensions	a = 10.777 ± 0.005 Å
	$\alpha = \beta = \gamma = 90°$
Volume	1251.68 Å^3
Z	4
Density (calculated)	4.221 g/cm^3
Reflections collected	3434
Unique reflections	82 from which 0 suppressed
R(int)	0.1109
R (sigma)	0.0266
Goodness-of-fit	1.151
Final R indices (R_{all})	0.0212
wR_{obs}	0.0322
Wavelength	0.71073 Å

Weight scheme for the refinement	Weight = 1/[sigma^2(Fo^2)+(0.0074 * P)^2+0.00*P] where P = (Max(Fo^2,0)+2*Fc^2)/3

Isotropic temperature factors (Å^2)	U_{iso} (Cs) 0.04284 ± 0.00044, (Bi) 0.02103 ± 0.00040 , (Ag) 0.02384 ± 0.00048, (Cl) 0.05063 ± 0.00107

Anisotropic temperature factor (Å^2)	U_{11}(Cs) = 0.04284 ± 0.00044, U_{11}(Bi) = 0.02103 ± 0.00040, U_{11}(Ag) = 0.02384 ± 0.00048, U_{11}(Cl) = 0.02039 ± 0.00149, U_{22}(Cs) = 0.04248 ± 0.00044, U_{22}(Bi) = 0.02103 ± 0.00040, U_{22}(Ag) = 0.02384 ± 0.00048, U_{22}(Cl) = 0.06567 ± 0.00152, U_{33}(Cs) = 0.04248 ± 0.00044, U_{33}(Bi) = 0.02103 ± 0.00040, U_{33}(Ag) = 0.02384 ± 0.00048, U_{33}(Cl) = 0.06567 ± 0.00152

Atomic Wyckoff-positions	Atom	Site	x	y	z	site occupancy
	Cs	8c	0.25	0.25	0.25	1
	Bi	4a	0	0	0	1
	Ag	4b	0.5	0.5	0.5	1
	Cl	24e	0.2489	0	0	1

Table S2: Crystallographic data for a $Cs_2BiAgBr_6$ single crystal.

Compound	$Cs_2BiAgBr_6$
Measurement temperature	293 K
Crystal system	Cubic
Space group	$Fm\bar{3}m$
Unit cell dimensions	a = 11.264 ± 0.005 Å
	$\alpha = \beta = \gamma = 90°$
Volume	1429.15 Å^3
Z	4
Density (calculated)	4.936 g/cm^3
Reflections collected	3830
Unique reflections	95 from which 0 suppressed
R(int)	0.0691
R (sigma)	0.0150
Goodness-of-fit	0.360
Final R indices (R_{all})	0.0192
wR_{obs}	0.0676
Wavelength	0.71073 Å

Weight scheme for the refinement	Weight = 1/[sigma^2(Fo^2)+(0.1874 * P)^2+0.00*P] where P = (Max(Fo^2,0)+2*Fc^2)/3

Isotropic temperature factors (Å^2)	U_{iso} (Cs) 0.05012 ± 0.00077, (Bi) 0.01985 ± 0.00051 , (Ag) 0.02820 ± 0.00071, (Br) 0.05347 ± 0.00066

Anisotropic temperature factor (Å^2)	U_{11}(Cs) = 0.05012 ± 0.00077, U_{11}(Bi) = 0.01985 ± 0.00051, U_{11}(Ag) = 0.02820 ± 0.00071, U_{11}(Br) = 0.02003 ± 0.00092, U_{22}(Cs) = 0.05012 ± 0.00077, U_{22}(Bi) = 0.01985 ± 0.00051, U_{22}(Ag) = 0.02137 ± 0.00296, U_{22}(Br) = 0.07019 ± 0.00083, U_{33}(Cs) = 0.05012 ± 0.00071, U_{33}(Bi) = 0.01985 ± 0.00051, U_{33}(Ag) = 0.02137 ± 0.00296, U_{33}(Br) = 0.07019 ± 0.00083

Atomic Wyckoff-positions	Atom	Site	x	y	z	site occupancy
	Cs	8c	0.25	0.25	0.25	1
	Bi	4a	0	0	0	1
	Ag	4b	0.5	0.5	0.5	1
	Br	24e	0.25091	0	0	1

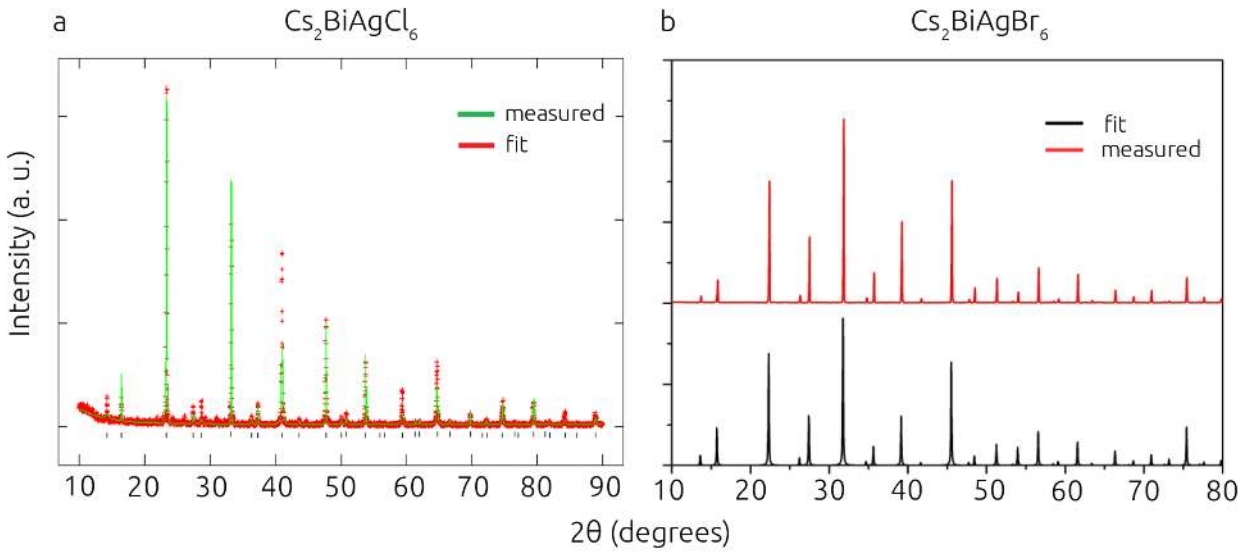

Figure S1: Powder X-ray diffraction spectrum for of $Cs_2BiAgBr_6$ measured at room temperature.

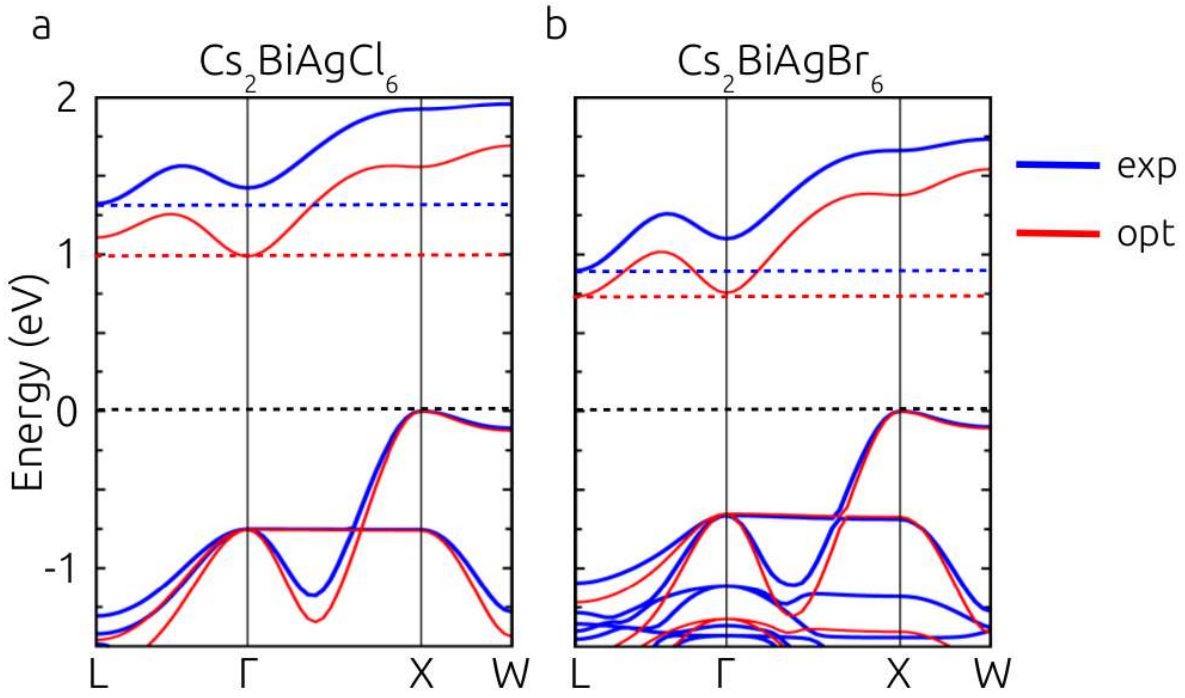

Figure S2: Comparison between the band structures of $Cs_2BiAgCl_6$ (a) and $Cs_2BiAgBr_6$ (b) calculated for the experimental (exp) crystal structures reported in Ref.[16] ($Cs_2BiAgCl_6$) and in Table S1 ($Cs_2BiAgBr_6$) and the optimized (opt) crystal structures. The dashed lines indicate the band edges (black for the valence band top in each case, red and blue for the conduction band bottom obtained from the calculation on the optimized and experimental crystal structures, respectively). The optimized crystal structures are obtained as described in Ref.[16]

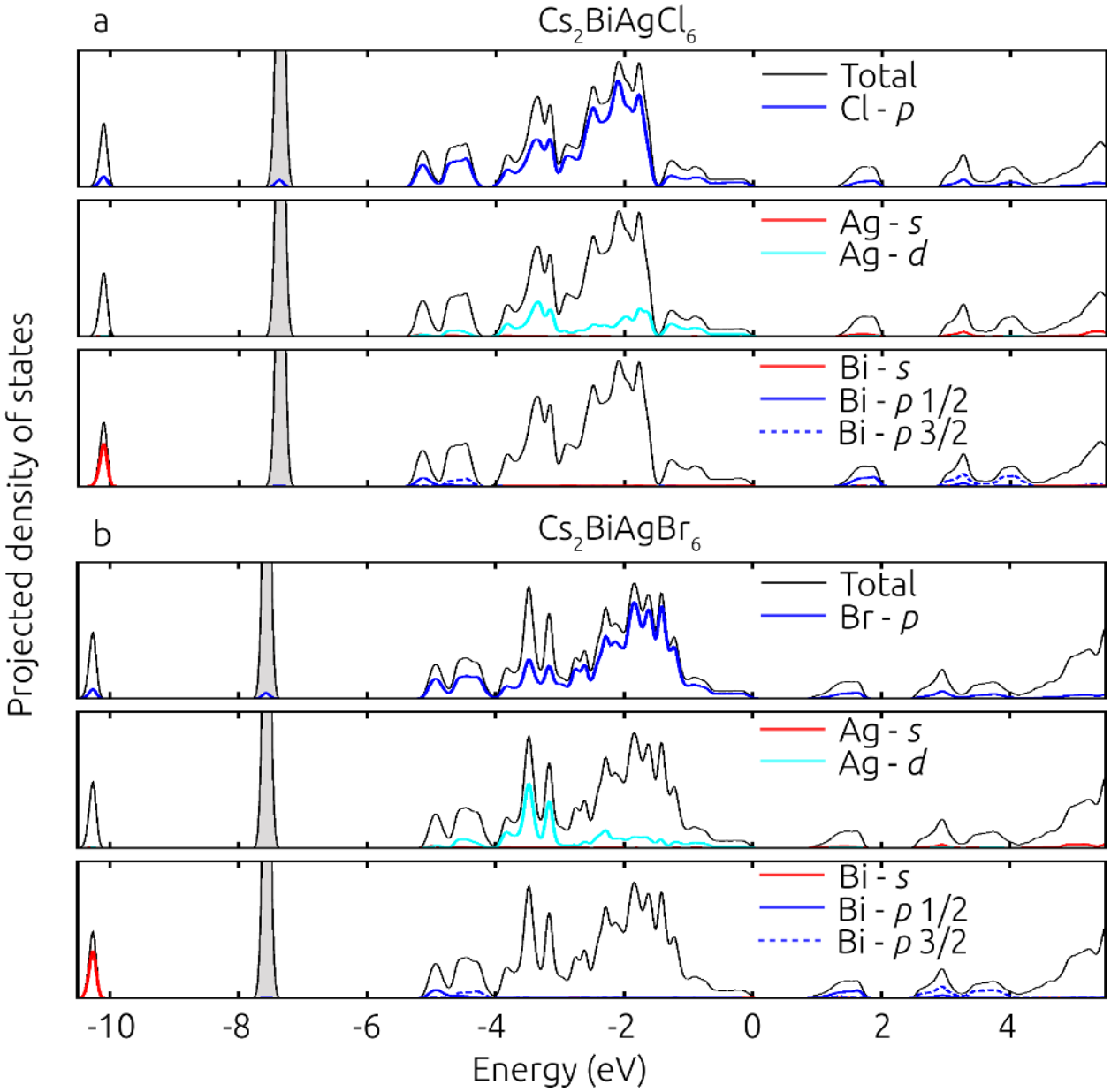

Figure S3: Projected densities of states calculated for $Cs_2BiAgCl_6$ (a) and $Cs_2BiAgBr_6$ (b) within DFT+SOC. The grey shaded peak appearing just above -8 eV in the valence band corresponds to the states localized on the Cs atom. The total density of states is plotted with a black line everywhere. Blue lines correspond to the p states, red lines correspond to the s states and light blue lines correspond to d states. These states are assigned to Bi, Ag, Cl or Br according to the legend. For Bi we distinguish between the spin-orbit split Bi p 1/2 (continuous line) and Bi p 3/2 (dashed line).

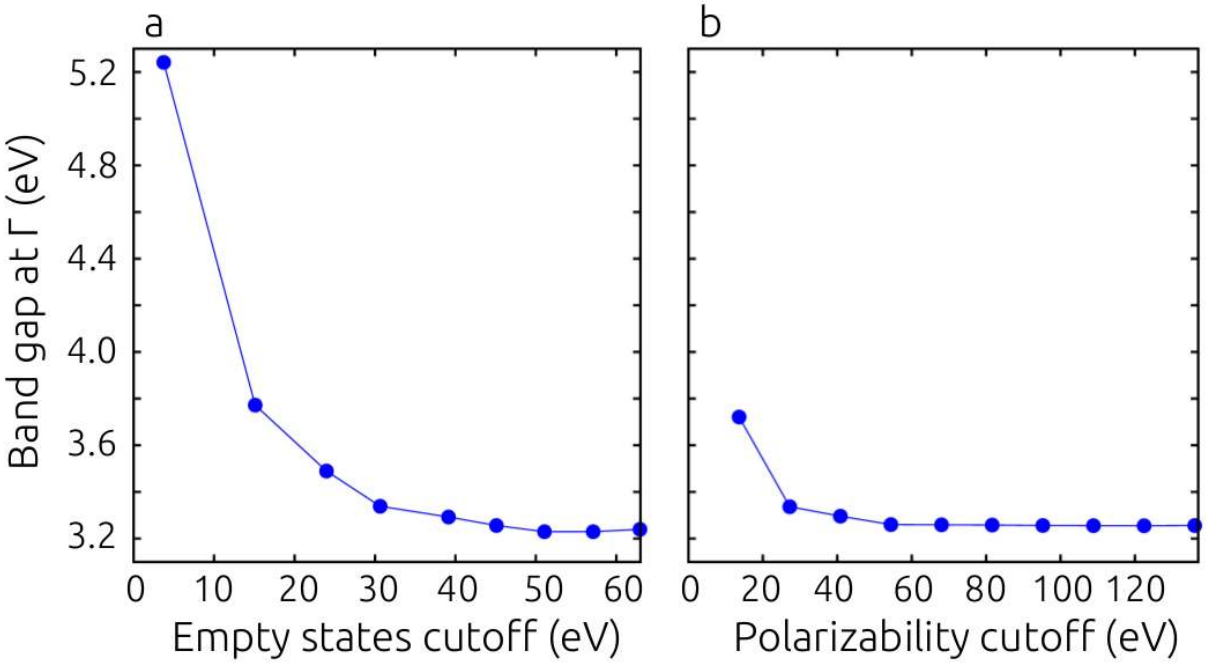

Figure S4: Convergence of the direct band gap at Γ with respect to the empty states cutoff (a) and polarizability cutoff (b) for $Cs_2BiAgCl_6$. All band gaps are obtained from calculations at Γ-point only using a polarizability cutoff of 95 eV for the convergence with the empty states (a) and an empty states cutoff of 45 eV (506 empty states) for the convergence with the polarizability cutoff.

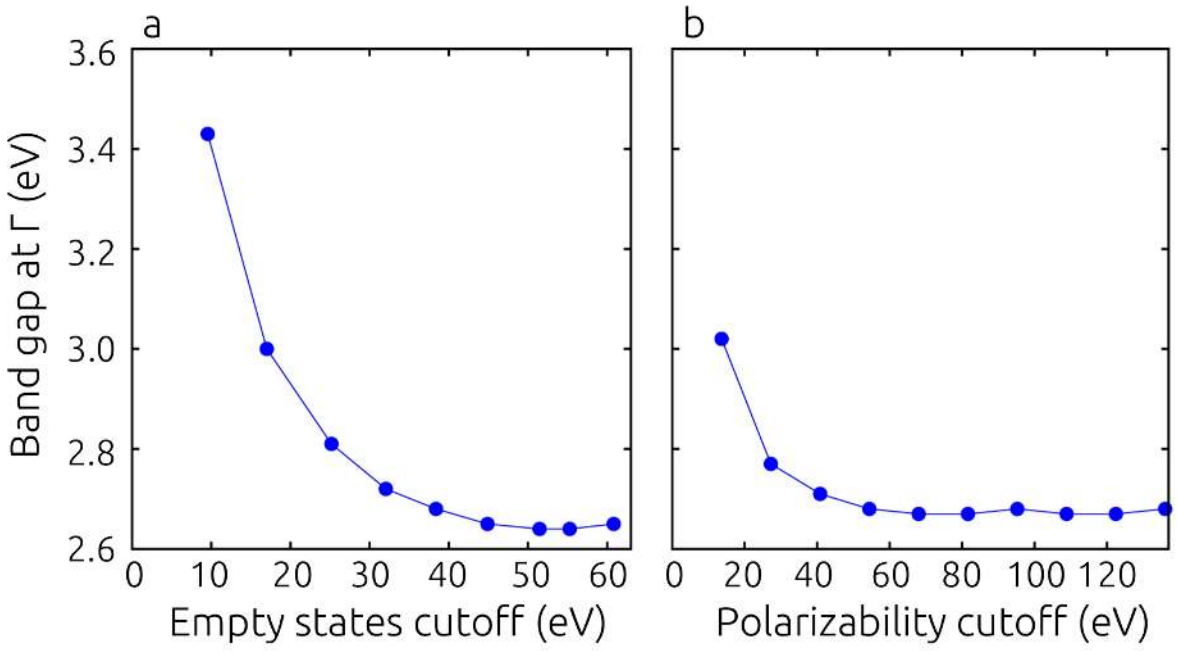

Figure S5: Convergence of the direct band gap at Γ with respect to the empty states cutoff (a) and polarizability cutoff (b) for $Cs_2BiAgBr_6$. All band gaps are obtained from calculations at Γ-point only using a polarizability cutoff of 95 eV for the convergence with the empty states (a) and an empty states cutoff of 42 eV (506 empty states) for the convergence with the polarizability cutoff.

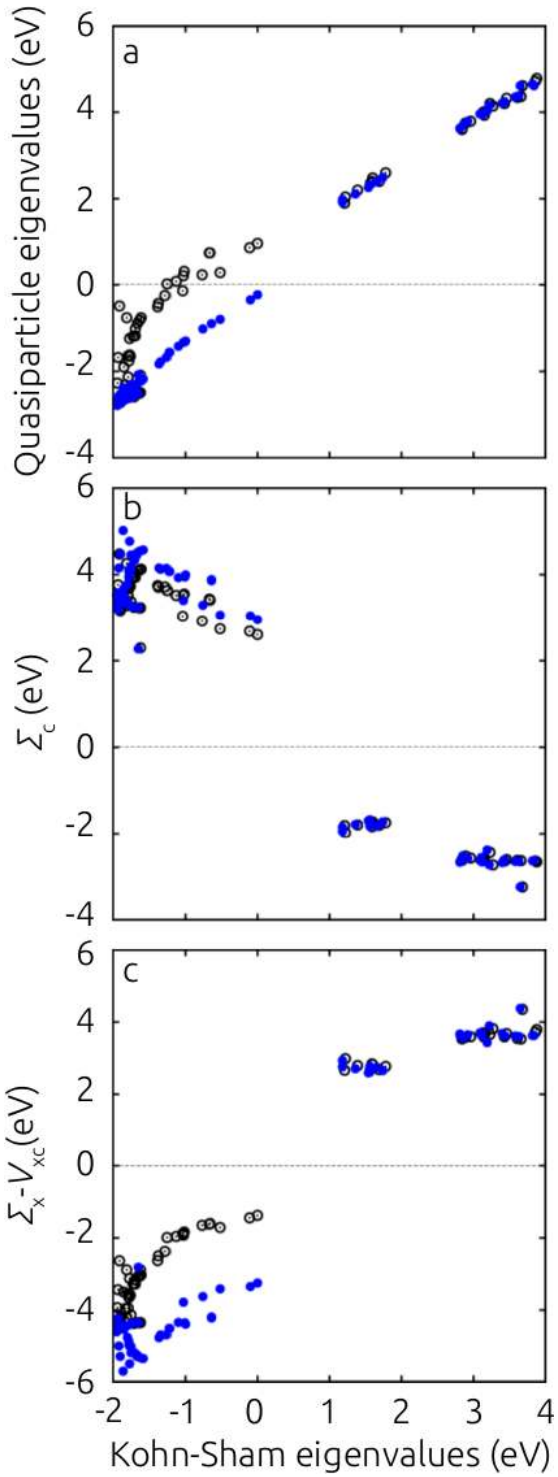

Figure S6: Plot of the quasiparticle energy (a), correlation self energy, Σ_c (b) and the difference between exchange self energy and the exchange-correlation potential, $\Sigma_x - V_{xc}$ (c) with respect to corresponding Kohn-Sham eigenvalues, for calculations without (empty black circles) and with (blue dots) semicore states for Ag. Both calculations are performed for $Cs_2BiAgCl_6$.

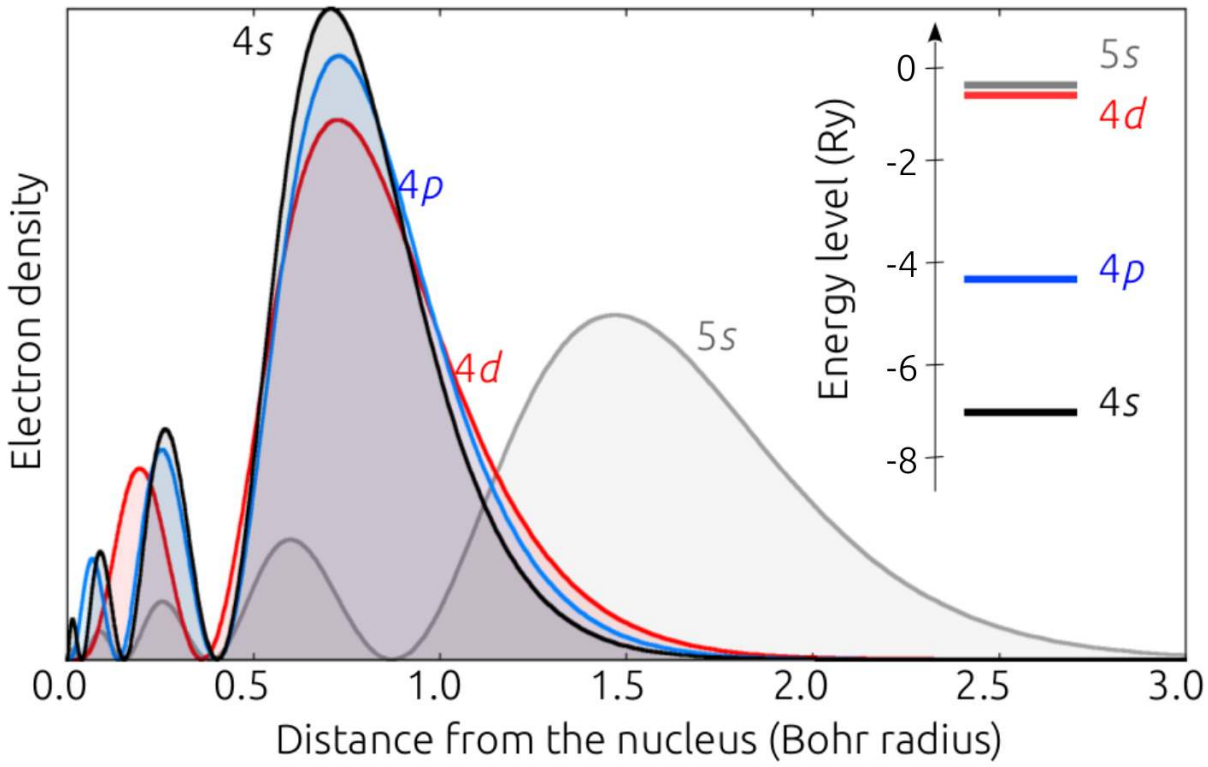

Figure S7: Overlap of the radial part of the $5s$, $4d$, $4p$ and $4s$ pseudo-atomic electron density of Ag as a function of the distance from the nucleus. The inset shows a schematic diagram of the energies of each orbital.

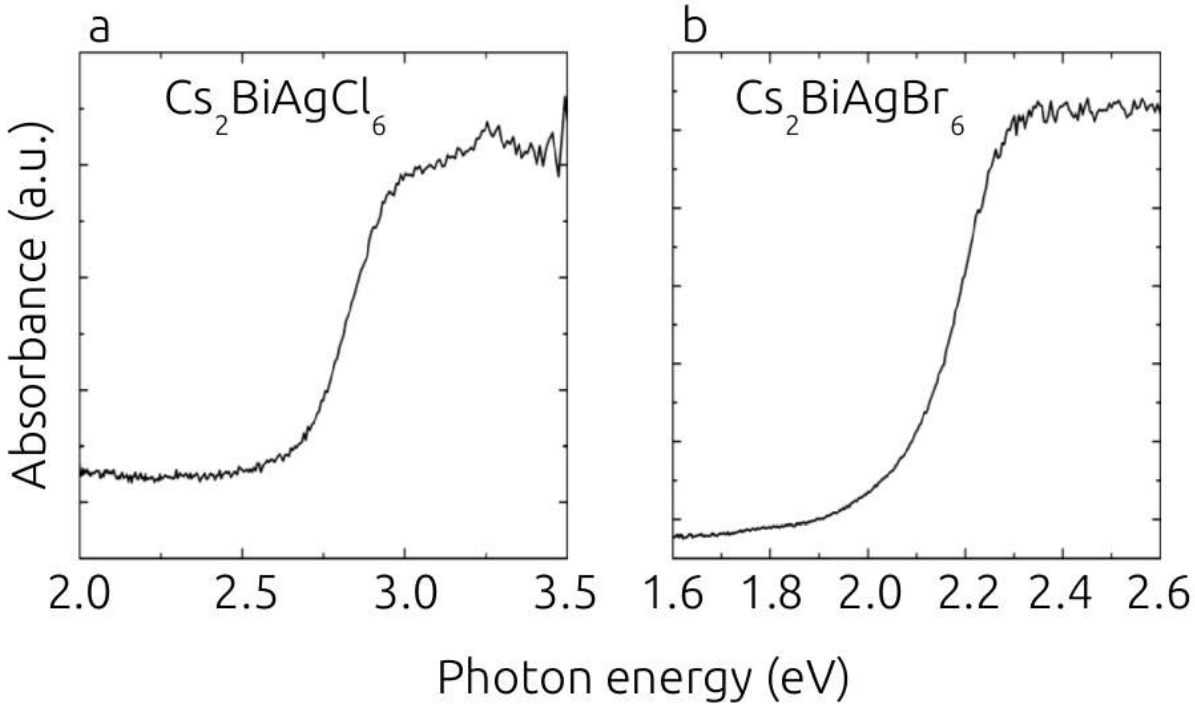

Figure S8: Room temperature optical absorption spectra of $Cs_2BiAgCl_6$ (a) and $Cs_2BiAgBr_6$ (b)

References

(1) Perdew, J. P.; Zunger, A. Self-Interaction Correction to Density-Functional Approximations for Many-Electrons Systems. *Phys. Rev. B* **1981**, *23*, 5048.

(2) Gianozzi, P.; Baroni, S.; Bonini, N.; Calandra, M.; Car, R.; Cavazzoni, C.; Ceresoli, D.; Chiarotti, G. L.; Cococcioni, M.; Dabo, I.; Dal Corso, A.; de Gironcoli, S.; Fabris, S.; Fratesi, G.; Gebauer, R. et al. QUANTUM ESPRESSO: A Modular and Open-Source Software Project for Quantum Simulations of Materials. *J. Phys.: Condens. Matter.* **2009**, *21*.

(3) Vanderbilt, D. Soft Self-Consistent Pseudopotentials in a Generalized Eigenvalue Formalism. *Phys. Rev. B* **1990**, *41*, 7892.

(4) Louie, S. G.; Froyen, S.; Cohen, M. L. Nonlinear Ionic Pseudopotentials in Spin-Density-Functional Calculations. *Phys. Rev. B* **1982**, *26*, 1738.

(5) Pseudopotentials. `http://theossrv1.epfl.ch/Main/Pseudopotentials`, accessed: September, 2015.

(6) Troullier, N.; Martins, J. L. Efficient Pseudopotentials for Plane-Wave Calculations. *Phys. Rev. B* **1991**, *43*, 1993.

(7) Hybertsen, M. S.; Louie, S. G. Electron Correlation in Semiconductors and Insulators: Band Gaps and Quasiparticle Energies. *Phys. Rev. B* **1986**, *34*, 5390.

(8) Aryasetiawan, F.; Gunnarsson, O. The *GW* Method. *Rep. Prog. Phys.* **1998**, *61*, 237.

(9) Giustino, F.; Cohen, M. L.; Louie, S. G. *GW* Method with the Self-Consistent Sternheimer Equation. *Phys. Rev. B* **2010**, *81*, 115105.

(10) Onida, G.; Reining, L.; Rubio, A. Electronic Excitations: Density-Functional Versus Many-Body Green's Function Approaches. *Rev. Mod. Phys.* **2002**, *74*, 601–659.

(11) Marini, A.; Hogan, C.; Grüning, M.; Varsano, D. Yambo: An Ab Initio Tool for Excited State Calculations. *Comp. Phys. Commun.* **2009**, *180*, 1392.

(12) Ceperley, D. M.; Alder, B. J. Ground State of the Electron Gas by a Stochastic Method. *Phys. Rev. Lett.* **1980**, *45*, 566.

(13) Adler, S. L. Quantum Theory of the Dielectric Constant in Real Solids. *Phys. Rev.* **1962**, *126*, 413–420.

(14) Godby, R. W.; Needs, R. J. Metal-Insulator Transition in Kohn-Sham Theory and Quasiparticle Theory. *Phys. Rev. Lett.* **1989**, *62*, 1169.

(15) Morrs, L. R.; Robinson, W. R. Crystal structure of $Cs_2BiNaCl_6$. *Acta Cryst. B* **1972**, *28*, 653–654.

(16) Volonakis, G.; Filip, M. R.; Haghighirad, A. A.; Sakai, N.; Wenger, B.; Snaith, H. J.; Giustino, F. Lead-Free Halide Double Perovskites via Heterovalent Substitution of Noble Metals. *J. Phys. Chem. Lett.* **2016**, *7*, 1254–1259.

(17) Larson, A. C.; Von Drele, R. B. General Structure Analysis System (GSAS). *Los Alamos National Laboratory Report LAUR* **2000**, 86–748.

(18) Sheldrick, G. M. Crystal Structure Refinement with SHELXL. **2015**, *71*, 3.